Computational Study of a Flow-Excited Helmholtz Resonator with Active Flow Control

A THESIS PRESENTED
BY
JACOB P. BUEHN
TO
THE DEPARTMENT OF MECHANICAL ENGINEERING

IN PARTIAL FULFILLMENT OF THE REQUIREMENTS
FOR THE DEGREE OF
MASTER OF MECHANICAL ENGINEERING
IN THE SUBJECT OF
MECHANICAL ENGINEERING

SAINT MARTIN'S UNIVERSITY
LACEY, WASHINGTON

MAY 2017

Thesis advisor: Professor Dr. Daniel R. Einstein Jacob P. Buehn

Computational Study of a Flow-Excited Helmholtz Resonator with Active Flow Control

Abstract

A computational study was performed of a flow-excited Helmholtz resonator. This setup was used to model the phenomenon that occurs when a sunroof is open, or rear passenger compartment window lowered, in an automobile. The results of the computational study were validated through comparison to experimental and numerical results found in literature. After validating the setup of the computational model through both qualitative and quantitative results, the research then focused on using methods of active flow control to reduce the sound pressure levels and fluctuations within the resonator. Specifically, this was accomplished through the use of a small elongated jet placed upstream of the resonator orifice. After seeing changes in the pressure levels using this active flow control technique, the velocity of the jet was altered to study its effect on the magnitude of pressure reduction. The final results from this computational study show the desired outcome of a reduction in pressure whose magnitude is dependent upon the jet velocity. It was concluded the mass air flow from the jet that is added to the boundary layer produces an effect similar to that of running the simulation at a higher free stream velocity, but without the active flow control jet. As an initial examination into the use of active flow control, using this simplified jet provides the ability to reduce pressure levels across a spectrum of free stream velocities.

Contents

Listing of figures

This thesis is dedicated to my parents, Pete and Marilyn Buehn, who always provided me with the opportunity to further my education. Thank you for allowing me to travel the path that has led to the work I have a passion for. Your wisdom and guidance has taught me so much through this process that I will be forever grateful for.

Acknowledgments

Thank you to my thesis advisors, Dr. Paul E. Slaboch of the University of Hartford and Dr. Daniel R. Einstein of Saint Martin's University. It was Dr. Slaboch who first introduced me to this research topic and the use of computational fluid dynamics. He was a trusted advisor and mentor throughout my master's level studies and this thesis research. He was instrumental in guiding me through the process of publishing a conference paper on this topic and presenting the work at an AIAA Aerospace conference. I am also very grateful to Dr. Einstein who came aboard as my advisor during the latter phases of my thesis work. His knowledge and background using CFD was instrumental in my ability to complete my thesis, as well as enhancing my own CFD skills. Thank you to both of my thesis advisors for the time and effort they invested into my education. My thanks also goes out to the entire staff of the mechanical engineering program at Saint Martin's University.

Symbols

c	Speed of sound
cfm	Cubic feet per minute
F^*	Non-dimensional hydrodynamic force
f	Frequency
f_{hr}	Resonator natural frequency
f_p	Peak frequency
G_{pp}	Autospectral density
L	Length of orifice opening
M	Mach number
P^*	Non-dimensional peak resonator pressure
S	Area of orifice
U	Free stream velocity
U^*	Non-dimensional free stream velocity
U_{jet}	Jet velocity
U^*_{jet}	Non-dimensional jet velocity
u	Streamwise velocity
V	Volume of resonator
ϱ	Density
ω_z	Spanwise vorticity
$\hat{}$	Fourier transformed variable

1

Introduction

1.1 Overview

This paper details a computational study that was performed of a flow-excited Helmholtz resonator with the purpose of evaluating active flow control techniques. The simple example of how a Helmholtz resonator works can be demonstrated with an empty glass bottle. As air is blown across the opening, an audible tone can be heard due to the pressure oscillating within the bottle. This is caused by the air

that is forced into and out of the bottle in a specific cyclic manner.

This same phenomenon—termed 'window buffeting'—occurs on a larger scale when an automobile traveling at speed has an open side window or sunroof, causing pressure oscillations within the cabin. When the automobile is traveling in a specific speed range, those pressure fluctuations can reach the point of causing audible discomfort. It is the purpose of this study to model the automobile as a Helmholtz resonator and use computational analysis in evaluating active flow control techniques intended to reduce the pressure levels.

1.2 Self-Excited Helmholtz Resonator

A schematic of grazing flow over a thin-walled Helmholtz resonator is shown in figure 1.1. The fundamental fluid mechanics of this phenomenon have been explored in great detail, most notably and recently by Ma et al.[9] The self-excited resonance is a result of a shear layer instability coupled to the Helmholtz resonator acoustics. The unsteady shear layer over the orifice periodically rolls up into discrete vortices that are subsequently convected downstream. When the vortices are ejected from the

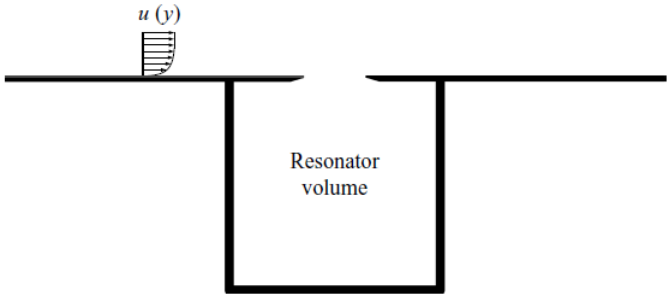

Figure 1.1: Schematic of grazing flow over a thin-walled Helmholtz resonator[9]

cavity at the downstream edge there are fluctuations in the total net circulation, leading to pressure oscillations in the resonator.[12]

A Helmholtz resonator can be modeled as a second order mass-spring-damper system, as shown in Figure 1.2. The compressibility and viscosity of air within the resonator cavity act as the spring and damper. The slug of air within the neck area is the mass oscillating into and out of the cavity.[9] It is important to note, for the phenomenon of a Helmholtz resonator the overall dimensions of resonator are much less than an acoustic wavelength.[13]

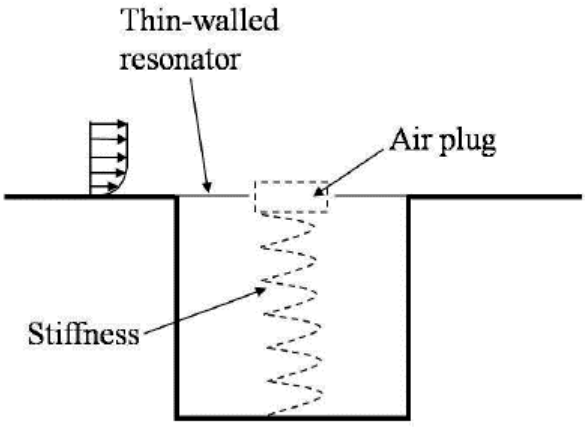

Figure 1.2: Schematic of Helmholtz resonator modeled as a second order mass-spring-damper system[9]

To evaluate different active flow control techniques that can be used to alter the pressure oscillations within the resonator, a computational model is used. To be confident in this computational fluid dynamics (CFD) model, a validation study was first performed with a model that did not use any type of flow control. The results were compared against known experimental and analytical results available in literature. Active flow control was then added without altering the physical parameters of

the computational model or solver settings used.

Grazing flow over a Helmholtz resonator poses a unique problem for a CFD study as flows at this speed ($M < 0.05$) are generally considered incompressible; however the coupled shear layer instability and cavity resonance create a weakly compressible flow, such that compressibility effects within the resonator cannot be ignored. Typically, computational studies about the type of Helmholtz resonator in this paper use an LES or hybrid-LES turbulence model, as opposed to the more common RANS-based models.[8] [4] However, the realizable $k - \varepsilon$ turbulence model used in the current study is RANS-based and has been able to accurately model the Kelvin-Helmholtz shear layer instability—producing the proper pressure oscillations within the resonator. The selection of the turbulence model will be discussed in greater detail in the Computational Setup chapter.

1.3 Literature Review

While the fundamental flow physics of Helmholtz resonators has been well studied, research into controlling the phenomenon has only recently become more prevalent as the use of CFD has become more accessible. A look into what has been achieved through passive control can give a starting point for what active control is trying to replicate and ultimately improve upon. Research already conducted with active control can provide useful insight for the current study about what has or has not been successful so far.

Research by Ma, Slaboch, and Morris. included both analytical and experimental analysis.[9] Further study by Slaboch–using the same experimental model–investigated the use of passive control devices

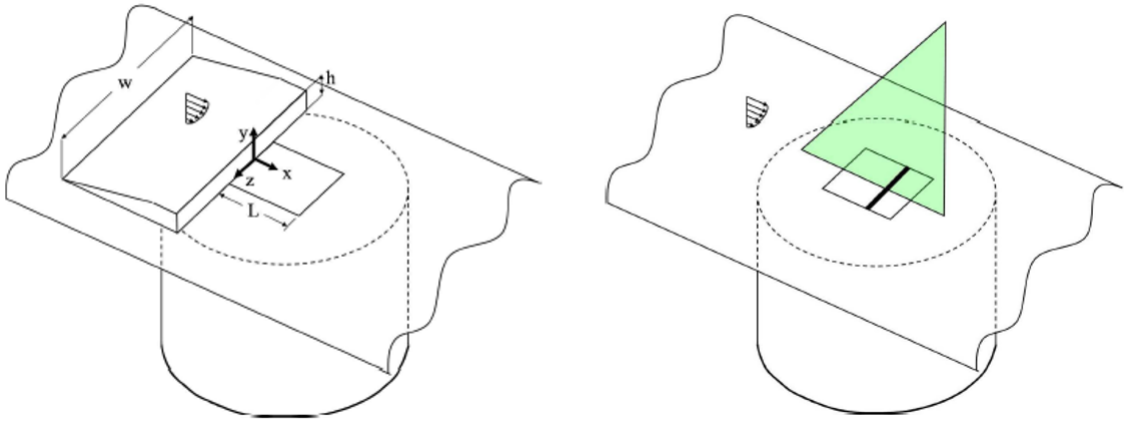

Figure 1.3: Passive control devices used by Ma et al.[16]

and alterations in characteristics of the orifice opening in the attempt to reduce the level of pressure oscillations. Figure 1.3 depicts two of these devices, including ramps located upstream of the orifice leading edge and spanwise slats placed across the orifice opening. Changes to the characteristics of the orifice included using a trapezoidal shaped orifice and altering the shape of the orifice edges.[16]

Computational studies presented by Mallick, Shock, and Yakhot use a similar geometry with numerical procedures based on the lattice kinetic equation. They combine this with the RNG turbulence model, similar to the widely used $k - \varepsilon$ model, while using the commercially available PowerFLOW software.[10] Also using this numerical method and software is Crouse et al., however their computational model includes a basic model of a full automobile. In relation to the Helmholtz resonator, the cabin represents the resonator and an open sunroof is the orifice opening.[6] Both of these studies produced good agreement between their computational results and physical experiments.

Utilizing a different numerical approach was Bai et al. whose computational model was also that

of a simplified car. Their use of computational aero-acoustics(CAA) included application of an LES turbulence model and a four-stage Runge-Kutta numerical method. They investigated the effects of both an open sunroof as well as an open side rear window. Results showed that at low flow velocities the sound pressure levels increased as the speed increased, but around 60kph (37mph) the sound pressure levels began to drop with further increases in flow velocities.[5]

Studies investigating the use of active control have shown multiple different ways to reduce pressure oscillations within the resonator. Similar to what is currently being used on some automobiles, Mongeau et al. used a small spoiler located at the leading edge of a sunroof. Their design additionally connected a loudspeaker to the spoiler. Being able to oscillate the spoiler in a controlled manner, they were able to reduce the acoustic pressures by up to 20dB.[12] Multiple studies have investigated the use of air injection to actively control a Helmholtz resonator, however they are primarily at higher Mach numbers ($\mathcal{M} > 0.5$) than those dealt with in this study and those seen in automobile applications.[14 17 11 18] A CFD study conducted by An et al. did evaluate the use of mass injection in the B-pillar of an automobile at lower Mach numbers. With a mass injection of 320*cfm*, they saw a reduction in the peak buffeting sound pressure level of 6dB.[3]

2

Computational Model

2.1 Computational Setup

2.1.1 Model Geometry

To accurately model the physics that were occurring within the Helmholtz resonator, a three-dimensional model was used in conjunction with the compressible Navier-Stokes equations. Figure 2.1 is a 2 dimensional depiction of the computational model's geometry that was used for both the validation study

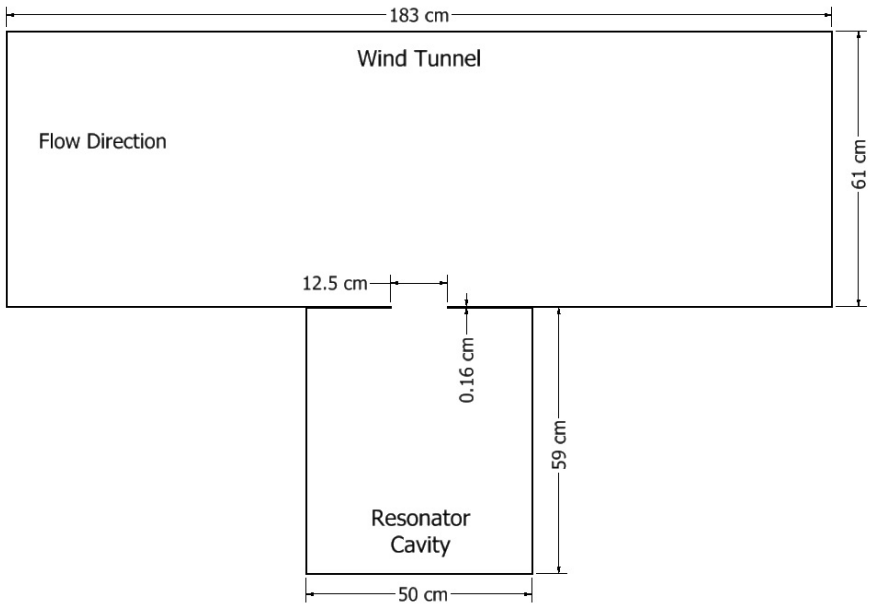

Figure 2.1: Schematic of geometry of interest with full tunnel

and active control research. The z-dimension is 50*cm* and the orifice opening is 12.5*cm* in both directions.

The model was created to replicate the wind tunnel, resonator, and orifice used by Ma et al. for their experimental research. Figure 2.2 shows the full 3D model with a reduction in the size of the wind tunnel. Due to limitations in computing resources, it was necessary to utilize every opportunity in minimizing the mesh count of the model. The wind tunnel was reduced in areas where it would not affect the flow physics of interest and a plane of symmetry was used to further reduce the size of the computational model. Initial simulations were run using both the full wind tunnel and that of the reduced version shown. Negligible differences in the results gave confidence in the use of the reduced tunnel without compromising accuracy of the results.

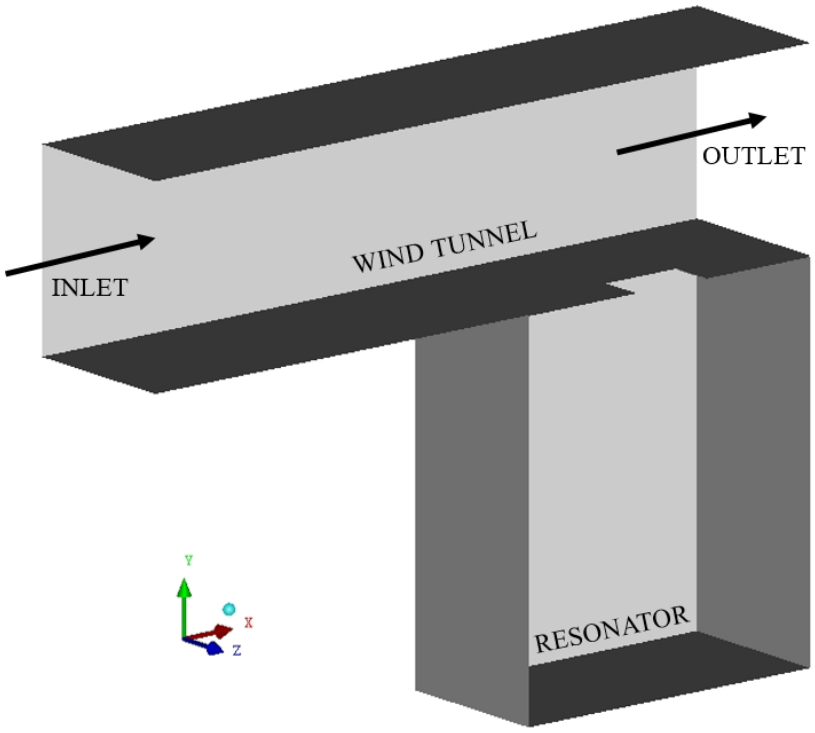

Figure 2.2: Schematic of 3d model with symmetry and reduced wind tunnel

2.1.2 Mesh Creation

Mesh creation and modification was done primarily with ANSYS ICEM CFD software and minor changes accomplished in Fluent. Based on the the geometry of the computational model, a structured mesh was used. This allowed changes in overall mesh density to be made while easily controlling the mesh size in the specific areas of the wind tunnel floor and resonator orifice. An example of the mesh used is shown in Figure 2.3, along with the increased mesh density for the tunnel floor boundary layer. The area surrounding the resonator orifice is depicted in Figure 2.3b and the mesh around the leading edge of the orifice in Figure 2.3c.

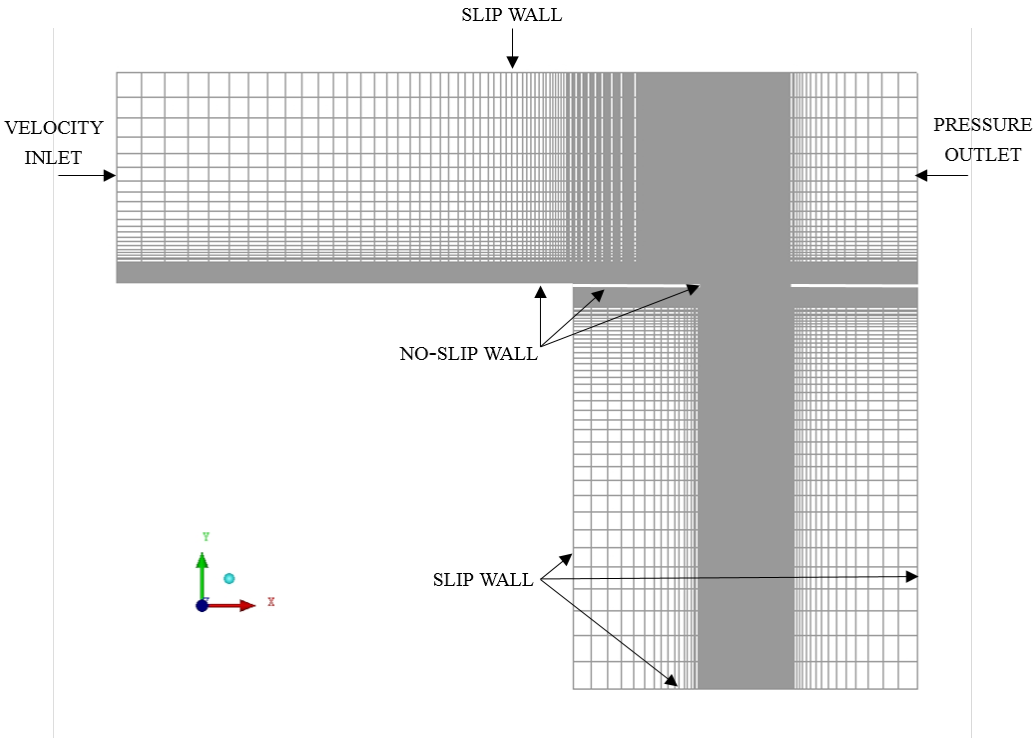

(a) Full CFD mesh with boundary conditions

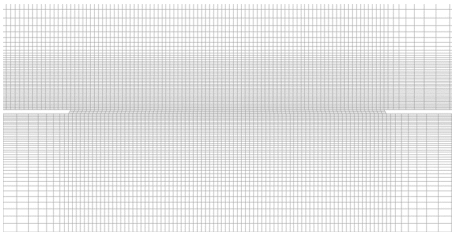

(b) Mesh around orifice opening

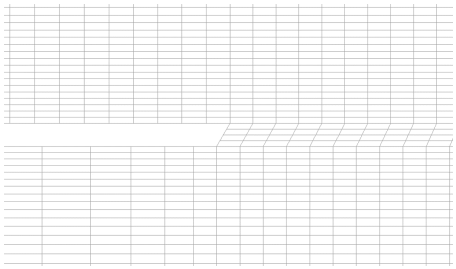

(c) Mesh around leading edge

Figure 2.3: Structured mesh and boundary conditions

A pressure monitor—located in the center of the resonator, 5cm up from the bottom—was used to record the pressure of the resonator at each time step. This mirrored the microphone setup from Ma et al's experimental work. During the simulations the pressure monitor recorded data at each time step that used to determine both the frequency and amplitude of pressure oscillations.

The mesh used for the validation study contained 3,340,973 elements. It was important to evaluate the quality of the mesh to ensure solution accuracy as well as stability of the numeric solver. These begin to degrade as the mesh elements deviate from their ideal shape. For this structured mesh, the ideal shape maintains 90° angles between all adjacent surfaces.

The region around the orifice is the only area where it was not possible to maintain this ideal shape. The original geometry used by Ma et al. utilized a knife edge that was 30° from horizontal on the leading and trailing edges of the orifice. To maintain the highest possible mesh quality in this area the knife edge was increased to 60°, producing elements with a parallelogram shape.

Maximum Orthogonal Quality: 0.8661 Range 0 to 1, values close to 0 correspond to low quality
Maximum Ortho Skew: 0.1339 Range 0 to 1, values close to 1 correspond to low quality
Maximum Aspect Ratio: 1.1004 exp 02

Table 2.1: Mesh Quality

Parameters of the mesh quality are listed in Table 2.1. The maximum orthogonal quality and maxi-

mum orthogonal skew are related as,

$$1 - \text{MaximumOrthogonalQuality} = \text{MaximumOrthogonalSkew}.$$

These are essentially a measure of the level of deviation of these parallelogram shaped elements from the ideal 90°.[2] The values shown in the table for these two parameters give confidence a quality mesh was maintained, despite the shape of elements around the knife edge.

The final parameter of mesh quality shown in the table is the maximum aspect ratio. This is a measure to compare the size of an element in each direction. The largest aspect ratio will occur in the boundary layer where the height of the element must be kept small, relative to other areas in the model. An aspect ratio too large will have an effect on solution accuracy and stability of the numerical solver, similar to the other mesh quality parameters.

2.1.3 Boundary Conditions

A depiction of the boundary conditions in Figure 2.3a shows a velocity inlet and pressure outlet used. While literature suggests the use of a typical pressure inlet/pressure outlet combination for compressible flow, it was determined for this specific, weakly compressible flow, a velocity inlet/pressure outlet combination was the most suitable.[2] The inlet was set to the desired free stream velocity while the outlet had an initial value of $0Pa$.

To reduce computational expense, all walls were set with slip conditions except the wind tunnel floor, resonator neck, and top interior of the resonator—where development of the boundary layers

would impact the results. The control volume surface was created on the plane of symmetry to record data of various parameters, as well as to visually inspect the flow properties within the area of the resonator orifice. However, the primary variable of interest was the pressure monitor located centrally in the bottom of the resonator.

2.2 Computational Solver

The solver used for the computational work was the commercially available software Fluent CFD developed by Ansys Inc. The validation and active control simulations were first run as steady state before switching to transient mode. It is important to first run as steady state to solve initially only for the flow, ignoring the transient effects. While the flow is ultimately time dependent, the steady state solution provides initial data from which the transient solution can compute the change in the variables as a function of time.

A coupled, pressure-based solver was used both for the steady state and transient simulations. As opposed to a segregated solver where the momentum equation and pressure-based continuity equation are solved separately, the coupled solver uses a single coupled system of equations.[1] The primary solver settings can be seen in Table 2.2.

The second order upwind numerical discretization scheme is used to solve for many of the continuity and scalar equations. This scheme is used to interpolate the scalar quantities from the cell center to the face of the cell. The term ”upwind” is used as the face values are derived from the cell center

Discretization	
Spatial	Least Squares Cell Based
Pressure	Second Order
Density	Second Order Upwind
Momentum	Second Order Upwind
Turbulent Kinetic Energy	Second Order Upwind
Turbulent Dissipation Rate	Second Order Upwind
Energy	Second Order Upwind
Transient Formulation	Second Order Implicit
Flow Courant Number	20
Explicit Relaxation Numbers	
Momentum	0.75
Pressure	0.75
Under Relaxation Factors	
Density	1
Body Force	1
Turbulent Kinetic Energy	0.8
Turbulent Dissipation Rate	0.8
Turbulent Viscosity	1
Energy	1

Table 2.2: Pressure-Based Solver Settings

upstream, relative to the direction of the normal velocity. The following equation is,

$$\varphi_f = \varphi + \nabla\varphi \cdot \overrightarrow{r}$$

where φ_f is the face value being evaluated, φ is the cell-centered value in the upstream cell, $\nabla\varphi$ is the gradient of that cell-centered value, and $\overrightarrow{r}$ is the displacement vector from the upstream cell center to the center of the face being evaluated.[1]

As shown in the table, the solver uses second order implicit temporal discretization. This means the time derivative is discretized using a second order method and the given variable's function is then evaluated using implicit time integration. The two possible methods for time integration are implicit or explicit—difference between the two lies in which time level of the dependent variable are used.

For implicit time integration, the following function is used to evaluate the variable at the next time step:

$$\varphi^{n+1} = \varphi^n + \Delta t F\left(\varphi^{n+1}\right)$$

This is implicit integration as the future value, φ^{n+1} in a specific cell is related to the future value in surrounding cells through the function $F\left(\varphi^{n+1}\right)$. An important aspect of this scheme is its ability to be unconditionally stable with respect to the size of time step.

Explicit time integration uses a similar function,

$$\varphi^{n+1} = \varphi^n + \Delta t F\left(\varphi^n\right)$$

however the dependent variable's future value, φ^{n+1} can be expressed solely in terms of the existing solution values, φ^{n}.[1]

The relaxation factors are also listed in Table 2.2. These are used when the solution becomes unstable or residuals begin to oscillate. By using the relaxation factors, the value of the specified variable used in the next iteration is reduced by the given factor amount. While being able to improve the stability of the system, lowering the relaxation factors will increase the number of iterations required. For the current study, the default values were used except for the explicit relaxation numbers for momentum and pessure that were reduced from 1 to 0.75.

Convergence criteria is used to help determine when the solution has achieved some type of unknown limit, giving confidence in the accuracy of the solution. For steady state simulations it is at this point the solution is said to have 'converged.' The steady state solution in the current study is only used as baseline initial data for the transient simulations. The fluid mechanics of the Helmholtz resonator are inherently unstable and will not reach a fully converged steady state solution.

To evaluate the solutions of the iterative process, specific convergence criteria are used. In both steady state and transient modes, the residuals of each quantity (mass, x-velocity, etc.) are evaluated after each iteration. Due to the finite volume method being used for discretization, the residual is a measure of the imbalance of the specific quantity within a finite volume.

There are then two ways to evaluate the residuals, absolute and relative. With absolute convergence, current residuals are evaluated against a user specified value. When all of the specified residuals have reached a value lower than these, the solution has converged. With relative convergence—available only for transient simulations—the residual of the current iteration is evaluated against the first itera-

tion of the time step being solved for. Once the difference between these two iterations is lower than the value set by the user, the solution is said to be converged and can move to the next time step.

Residual	Absolute	Relative
Continuity	0.0001	0.01
X-Velocity	0.001	0.05
Y-Velocity	0.001	0.05
Z-Velocity	0.001	0.05
Energy	1.0 exp −06	0.05
Turbulent Kinetic Energy	0.001	0.05
Turbulent Dissipation Rate	0.001	0.05

Table 2.3: Convergence Criteria

Table 2.3 shows the convergence criteria settings used. When running as steady state, only the absolute convergence criteria was used. It typically required around 500 iterations for the solution to converge. When running the transient simulations, both the absolute and relative convergence criteria were used with either being sufficient for the solution to converge. Each time step was allowed a maximum of 15 inner iterations, with convergence typically occurring around iteration 10-12.

The time step for transient simulations was 0.001 sec. This value was determined by running simulations at time steps ranging from 0.0005-0.002 sec. The initial value of 0.002 sec was the time step used by An et al. in their computational study of rear window buffeting.[3] When the simulations were ran with a time step smaller than 0.001 sec there was negligible change in the results. Therefore the

largest time step possible was used to conserve computational resources, while still providing accurate results. With a Helmholtz frequency of $47.8Hz$, this time step provided approximately 21 data points within each period of oscillation. This also agreed with what was found in additional literature, regarding an adequate time step for this type of flow problem.[19]

2.3 Turbulence Model

One of the most important aspects for an accurate computational model is in the selection of the turbulence model. The importance derives from the effect the turbulence and boundary layer have on the Kelvin-Helmholtz shear layer instability and its production of the pressure oscillations within the Helmholtz resonator. The accuracy of the turbulence model is generally relational to the computational resource it requires.

As mentioned in the Introduction the most favorable and common turbulence model used for a weakly compressible flow, such as the one in the current study, is an LES or hybrid-LES model.[8] [4] In relation to computational resource the LES model falls between a Direct Numerical Simulation(DNS), where all of the turbulence eddies are computed, and RANS-based models which use the Reynolds averaged Navier-Stokes equations. The hybrid-LES approach combines a RANS and LES model in various ways, with the outcome of reducing computational resources and maintaining the accuracy that would come from using a full LES turbulence model.

With the LES turbulence models, the turbulent flow is computed down to the scale of the large, energy containing eddies. Results are obtained given that the energy tends to travel from the larger

eddies down the energy cascade to the smallest eddies, but not in the reverse order. Those small eddies are not discounted completely though, as a heuristic model is used in the LES simulation to account for them.[7] While typically more accurate than a Reynolds-averaging turbulence model, the computational resources required made them still prohibitive with the computing resources available for the current study. To use an LES type turbulence model, the spatial resolution of the mesh would result in a mesh count an order of magnitude larger than the one used in this study.

The most widely used turbulence models use both empirical and exact equations to model the entirety of the turbulence, from the smallest to largest eddies. The $k - \varepsilon$ model is one of these such models. The name is derived from the variables that are used to represent the turbulent properties of the flow—the turbulent kinetic energy, k, and the turbulent dissipation rate, ε. The turbulence model found to be adequate for the current computational study was the realizable $k - \varepsilon$ model. This turbulence model is a relatively new enhancement to the standard $k - \varepsilon$ model. It was developed by researchers at the NASA Lewis Research Center in 1994.[15] While this model does still use wall models to model the turbulence, there are key improvements in this new realizable $k - \varepsilon$ model over the standard $k - \varepsilon$ model.

There are two important differences, the first is the formulation of the turbulent viscosity. In the standard model, the turbulent viscosity is computed from the following equation,

$$\mu_t = \varrho C\mu \frac{k^2}{\varepsilon}$$

with C_μ as a constant. In the realizable $k - \varepsilon$ model, C_μ is a variable and computed from

$$C_\mu = \frac{1}{A_0 + A_S \frac{kU^*}{\varepsilon}}$$

with

$$U^* = \sqrt{S_{ij}S_{ij} + \tilde{\Omega}_{ij}\tilde{\Omega}_{ij}}$$

and

$$\tilde{\Omega}_{ij} = \Omega_{ij} - 2\varepsilon_{ijk}\omega_k$$

$$\Omega_{ij} = \bar{\Omega}_{ij} - \varepsilon_{ijk}\omega_k$$

where $\hat{\Omega}_{ij}$ is the mean rate-of-rotation tensor with the angular velocity ω_k. As opposed to being a constant in the standard $k - \varepsilon$ model, C_μ is now a function of the mean strain and rotation rates, angular velocity of the system rotation, turbulent kinetic energy, and turbulent dissipation rate.

The second improvement is the dissipation rate's transport equation is now derived from an exact equation. The updated transport equations for k and ε are

$$\frac{\partial}{\partial t}(\varrho k) + \frac{\partial}{\partial x_j}(\varrho k u_j) = \frac{\partial}{\partial x_j}\left[\left(\mu + \frac{\mu_t}{\sigma_k}\right)\frac{\partial k}{\partial x_j}\right] + G_k + G_b - \varrho\varepsilon - Y_M + S_k$$

and

$$\frac{\partial}{\partial t}(\varrho\varepsilon) + \frac{\partial}{\partial x_j}(\varrho\varepsilon u_j) = \frac{\partial}{\partial x_j}\left[\left(\mu + \frac{\mu_t}{\sigma_\varepsilon}\right)\frac{\partial \varepsilon}{\partial x_j}\right] + \varrho C_1 S_\varepsilon - \varrho C_2 \frac{\varepsilon^2}{k + \sqrt{\nu\varepsilon}} + C_{1\varepsilon}\frac{\varepsilon}{k}C_{3\varepsilon}G_b + S_\varepsilon$$

with

$$C_1 = max\left[0.43, \frac{\nu}{\nu+5}\right], \nu = S\frac{k}{\varepsilon}, S = \sqrt{2S_{ij}S_{ij}}$$

G_k represents the generation of turbulence kinetic energy due to the mean velocity gradients, G_b is the turbulence kinetic energy generated due to buoyancy and Y_M represents the contribution of the fluctuating dilation in compressible turbulence to the overall dissipation rate. C_2, and $C_{1\varepsilon}$ are constants. The turbulent Prandtl number for the turbulent kinetic energy is represented by σ_k and for the turbulent dissipation by σ_ε. S_k and S_ε are user-defined source terms.[115]

As will be shown by the results of the validation study, the realizable $k-\varepsilon$ turbulence model has proved to be adequate for this computational study. There are also multiple computational studies of similar, basic, flow fields that use the standard $k-\varepsilon$ turbulence model[6 10]. This inspired confidence in the use of the realizable $k-\varepsilon$ turbulence model as it has been found to be substantially better than the standard $k-\varepsilon$ model.

3

Validation Study

The purpose of this study was to provide an initial look into the use of active control using a computational model. Prior to adding active flow control to the computational model, a validation study and grid independence study were performed to gain confidence in the results obtained using CFD. The validation study was executed by comparing the baseline computational results to the analytical and experimental results reported in the work done by Ma et al.[9] While the active control study was

performed for a single specific free stream velocity, the validation study evaluated multiple free stream velocities.

Given the limitations of the computational resources available, certain assumptions and compromises were made throughout the study. These included the reduction in wind tunnel size discussed earlier, the use of a RANS based turbulence model, and slip walls being used away from the area of interest. For this reason the validation study is important to ensure the computational model and CFD settings were correct, the turbulence model was able to handle the unsteady flow regimes, and the code was able to accurately compute the flow physics of the Helmholtz resonator.

3.1 Validation Parameters

For comparison purposes, three specific parameters presented by Ma et al. were chosen, P^*, F^*, and vorticity levels. A majority of their results are presented in non-dimensional form so as to be easily applicable to Helmholtz resonators of any size or geometry.[9] For the present study, those quantitative parameters are combined with qualitative inspection of the flow structures to evaluate the results of the computational analysis. The same parameters are then used in evaluating the effectiveness of active control in the following chapter.

The primary goal with the use of active control is to reduce the pressure levels within the cabin of the automobile, which is represented by the resonator in this study. For this reason the value of P^*, which is the non-dimensional peak pressure within the resonator, is important for validation as well as for evaluation of the active control results. In the computational model the pressure is measured

at a monitor point located in the center of the resonator, $5cm$ from the resonator bottom; the same location as the microphone in the Ma et al. experiments.[9] The pressure signal was formulated by logging the pressure data as a function of time. To then obtain P^*, the autospectral density of the pressure signal can be integrated in the following manner

$$P^* = \frac{2}{\varrho U^2}\left[\int_{0.8f_p}^{1.2f_p} G_{pp}(f)\,\mathrm{d}f\right]^{1/2},$$

where ϱ is the density, U is the free stream velocity, f_p is the peak frequency, and G_{pp} is the autospectral density. The non-dimensional free stream velocity U^* is found from $\frac{U}{f_{hr}L}$. The length of the orifice opening is L and the resonator natural frequency is $f_{hr} = \left(\frac{c}{2\pi}\right)\sqrt{\frac{S}{Vl}}$, with S the area of the orifice, V the volume of the resonator, l the effective neck thickness, and c the speed of sound.[9]

To compute the value of P^*, the resonator pressure signal from the simulation was used as an input into a custom MatLab program. This was used to obtain the resulting peak frequency, P^*, $\log P^*$, and a SPL plot (discussed in the following section) for any free stream velocity, orifice size, or Helmholtz frequency. The program also allowed the user to evaluate the pressure signal plot and select the portion to be used. This is necessary as the data at the start of the simulation, prior to the pressure reaching a maximum level, need discarded before the pressure signal could be used in any calculations.

The second parameter used for validation from Ma et al.'s experimental and numerical work was the non-dimensional hydrodynamic forcing term, F^*. The control volume used in the calculation of F^* is shown in Figure 3.1. Obtained by integrating the velocity-vorticity product over the control

volume, F^* was developed by Ma et al. and is expressed as,

$$F^* = \frac{\int \varrho(u\omega_z)\hat{}\,\mathrm{d}A}{\frac{1}{2}\varrho U^2 L}$$

where ϱ is the density, u is the streamwise velocity, ω_z is the spanwise vorticity, U is the free stream velocity, L is the length of the orifice, and A is the control volume area around the orifice opening.[9] The $\hat{}$ symbol indicates a fourier transformed variable.

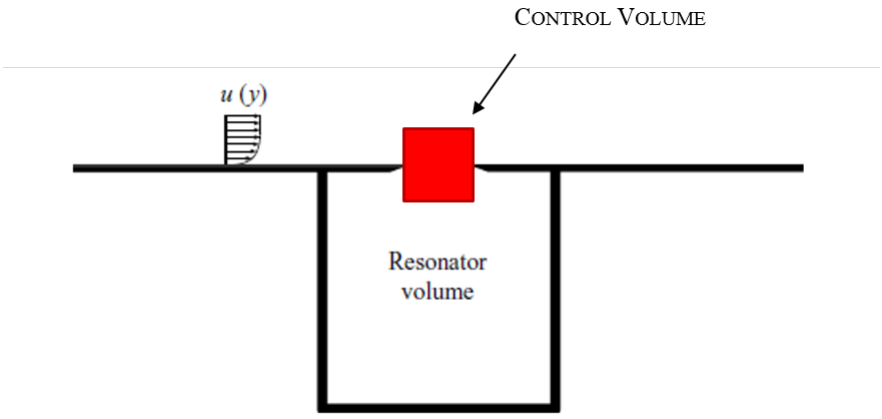

Figure 3.1: Control volume used for F^* calculation

3.2 Validation Study Results

3.2.1 Vorticity levels and contour plots

Comparing vorticity contours to the experimental work provided an initial assessment that the proper flow physics were being produced in the computational simulations. The general flow physics and what the vorticity would look like was known from experimental work found in literature. This initial

assessment was important to validate the ability of the realizable $k-\varepsilon$ turbulence model to accurately model the unsteady flow regimes and produce the vorticity at the orifice leading edge. The computational study was also able to depict the vortical structures in 3 dimensions. Previous research found in literature was limited to depicting the vorticity in 2 dimensions.

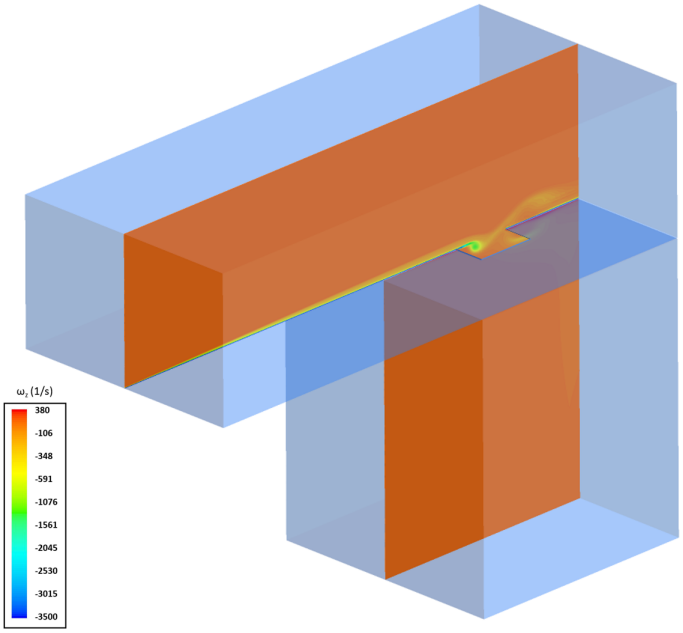

Figure 3.2: 3d model with Z-Vorticity contour plot on plane of symmetry

The transparent computational model in Figure 3.2 is shown with a contour plot of z-vorticity on the plane of symmetry. The images in Figure 3.3 have an iso-surface of z-vorticity at $\omega_z = -200(1/sec)$. The turbulent kinetic energy contours on the surface are used to better illustrate the vortical structures. As expected there is a discrete vortex spanwise across the orifice that is being convected downstream. This 3-dimensional model is able to show a noticeable amount of vorticity rolling over from the sides of the orifice, effecting the uniformity of the vortex.

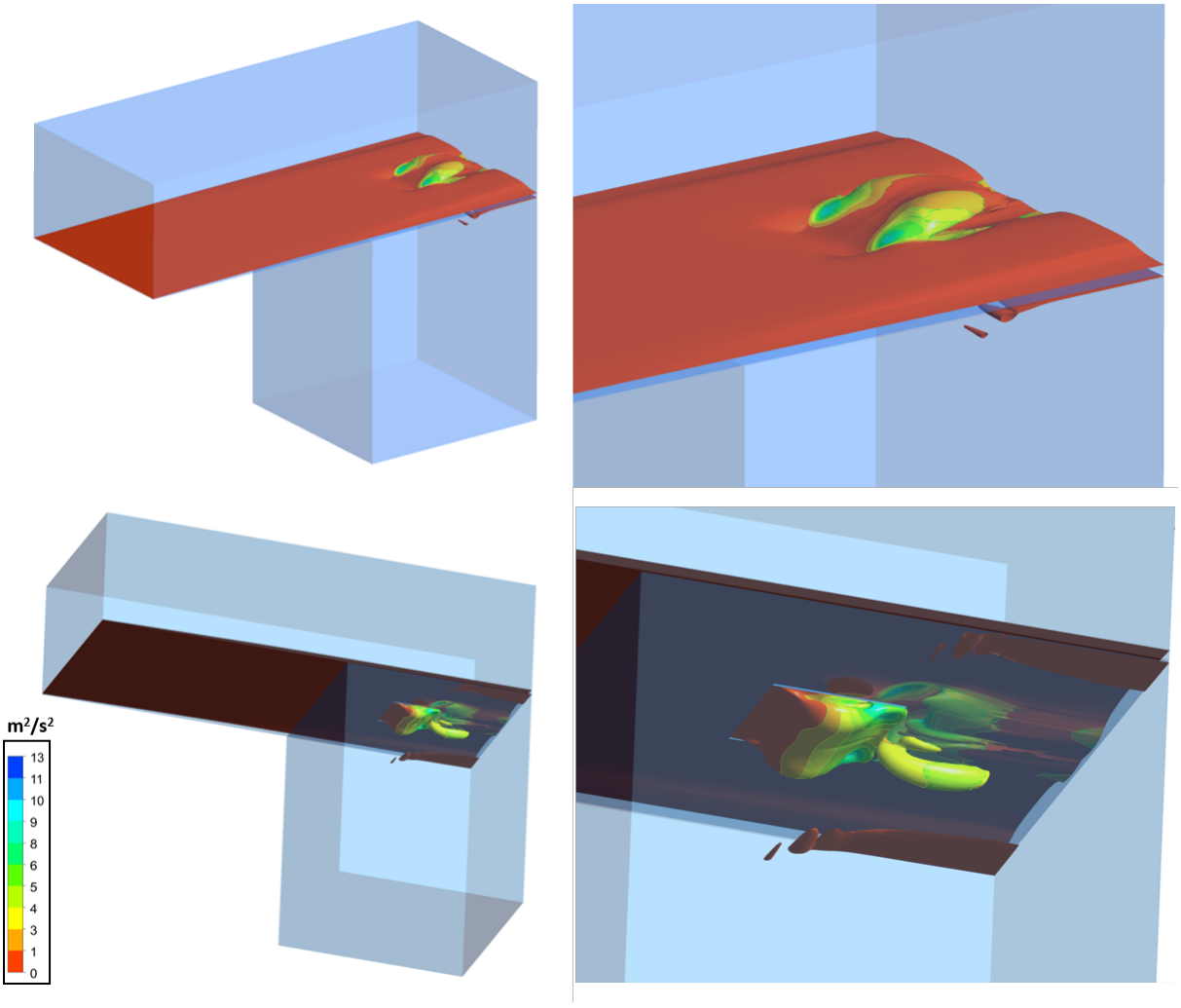

Figure 3.3: 3d model with $\omega_z = -200(1/sec)$ iso-surface and turbulent kinetic energy contours

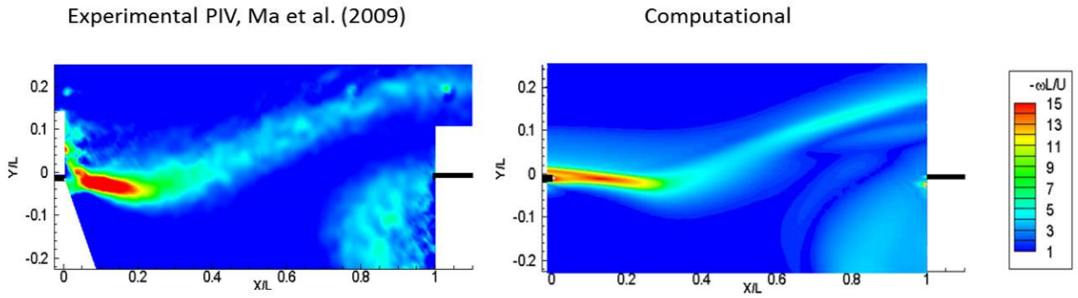

(a) Phase angle $\pi/2$

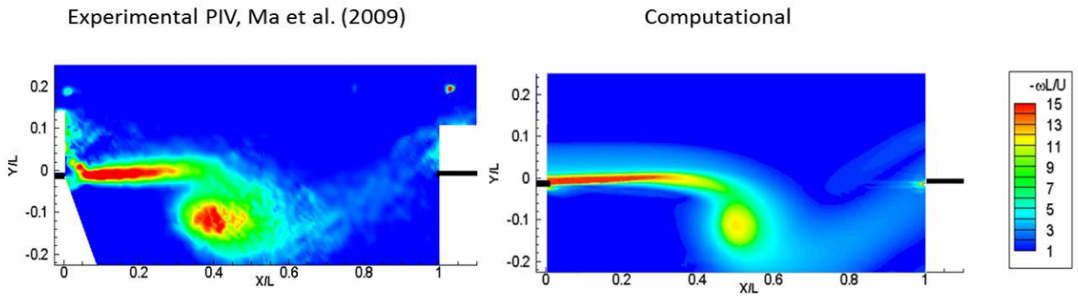

(b) Phase angle $3\pi/2$

Figure 3.4: Contours of spanwise vorticity at two different phase angles. Computational results are compared to the experimental results of Ma et al [9]

Figure 3.4 shows vorticity in the area of the resonator orifice at two different phases angles. The images on the left are experimental particle image velocimetry (PIV) phase averaged images from Ma et al.[9] Those on the right are from the present computational study. Both are shown at two different phase angles of the period of oscillation, $\pi/2$ in Figure 3.4a and $3\pi/2$ in Figure 3.4b. Additionally, the vorticity levels of the computational contour plot were converted into non-dimensional form to match how the vorticity is shown in the experimental PIV contour plots.

Agreement between the PIV results and the present study show the flow physics produced by the

computational simulations are qualitatively the same as the experimental flow physics. Inspecting the vorticity contour plots, the vorticity rolls up approximately halfway across the orifice at which point it detaches from the shear layer and convects downstream. Meanwhile, the shear layer is forced upwards due to the increased resonator pressure and a jet of irrotational flow is expelled from the resonator.

Aside from the purely qualitative aspects of the flow, the quantitative parameters are also used for validation. It can be seen in Figure 3.4 the vorticity levels are nominally the same between the experimental and computational plots at every point in the flow. The results are not exactly the same however, with some of the differences attributed to the fact that the images from Ma et al. are a composite image of approximately 100 individual realizations at nominally the same phase angle. Those images were spread out over 36° of phase and averaged to create the single composite image.[9] The current computational results are not averaged as each phase angle shown is a single snapshot in time.

The spatial resolution is also higher in the current simulations than in the PIV results, which can have an impact on the visual definition of the vorticity contour plot. The computational results originate from a simple square control volume. The contour plot image was then cropped on the top and bottom to match the height of the PIV contour plot image. This did not effect either the qualitative or quantitative results, but allowed easy comparison between experimental and computational contour plots. The control volume of the experimental results has the shape that is shown due to the necessary positioning of the multiple cameras used in the PIV experiment, with the combined data used to produce the experimental contour plot shown.[9]

3.2.2 Quantitative Parameters

For this specific resonator and neck geometry the experimental natural frequency, also termed Helmholtz frequency, was measured by Ma et al. to be 46 Hz.[9] When the computational study was run at $U^* = 2.64$, the frequency was found to be $47.8Hz$. While the results show good agreement, the difference could be attributed to small variations in the computational model when compared to the experimental model. As discussed in the previous chapter, the knife edge in the computational model was changed from 30° to 60°. Also, the walls of the resonator are treated as rigid walls in the computational study. In the experimental study it is possible there was a small amount of flex of the walls. These two differences could effect the results as the Helmholtz frequency is in part a function of the neck geometry and resonator volume.

Figure 3.5 presents the computational results of P^* at various free stream velocities, compared to the analytical and experimental results of Ma et al.[9] In their work, the peak amplitude pressure fluctuations were found to occur at $U^* = 2.64$; this was also obtained in the computational results. The comparison between the experimental and computational results shows good agreement. At the free stream velocity where peak pressures occur, the computational P^* was found to be within 1.2% of the experimental value. At two additional speeds, one lower and one higher than peak, the computational value was found to be within 3.1% and 11.8%, respectively.

While the computational results were further from the experimental results at off-peak values, the overall comparison is still within acceptable bounds for this preliminary type of study; most notably due to the fact that the present active control study was conducted solely at the peak P^* free stream

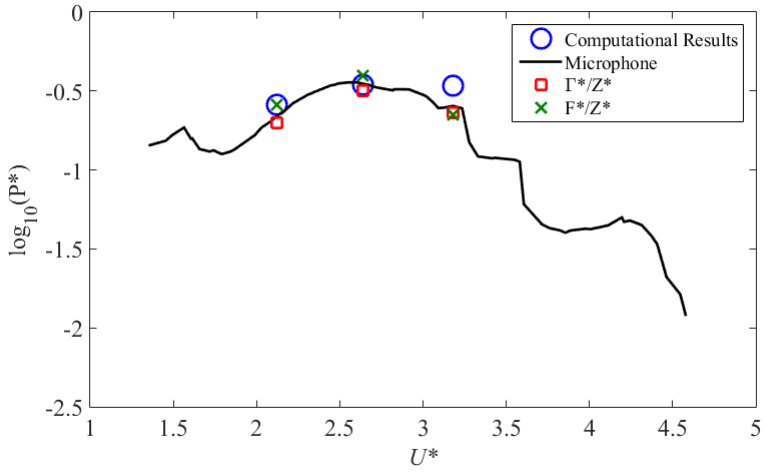

Figure 3.5: Validation study P* results

velocity, where the computational and experimental results match well. Additionally, the increased difference at higher U^* values can be attributed to the computational setup. The mesh and time step were optimized for running at the range of the peak P^* values. Changes in mesh density could effect the results when run at higher free stream velocities.

Evaluating the second validation parameter, the computational study resulted in $F^* = 0.038$ at $U^* = 2.64$. This is compared to the average value of 0.032 calculated by Ma et al. from their experimental results. They also evaluated five other experimental studies whose data were available in literature. From those data sets a mean value of 0.036 was found, with a standard deviation of 0.008.[9] It can be seen that the results of the current computational study fall within the range of what would be expected, given the experimental results listed above.

Figure 3.6 depicts the control volume used in the evaluation of F^*. The contour plot shown is an example of the spanwise vorticity used in its calculation. A custom MatLab program used data from

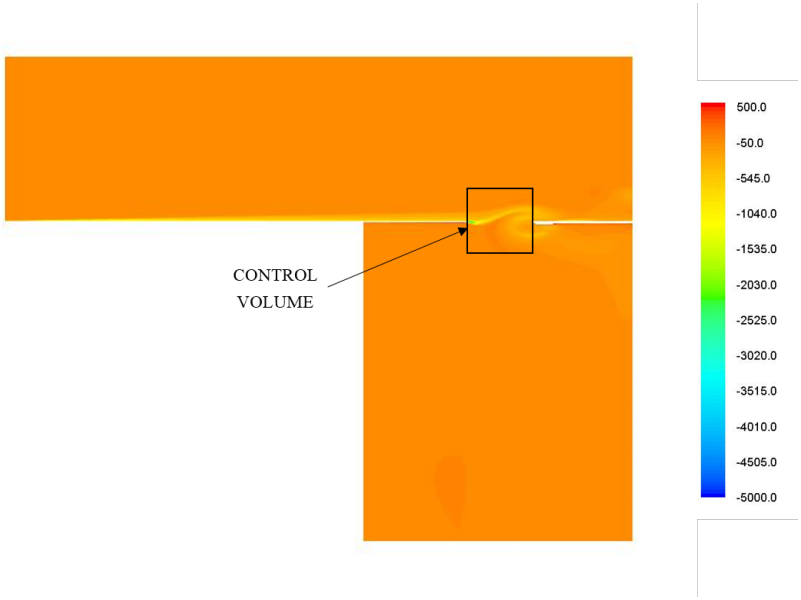

(a) Plane of symmetry

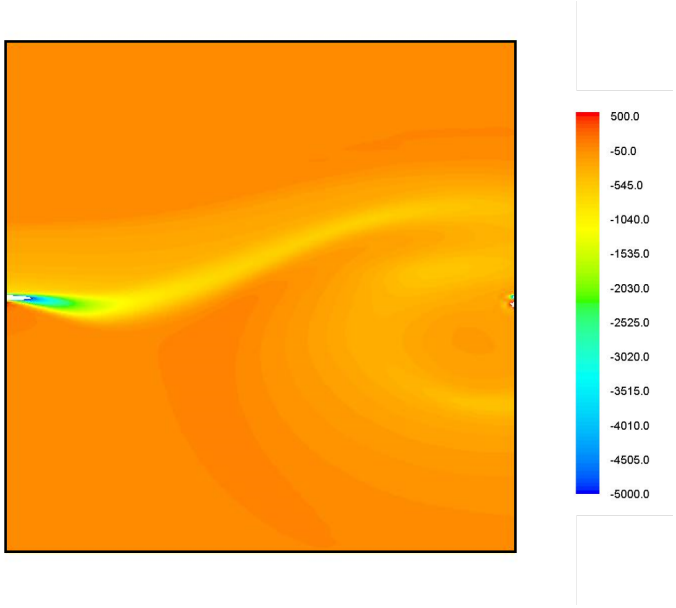

(b) Control volume used for calculations

Figure 3.6: Spanwise vorticity $\left(\frac{1}{sec}\right)$ at phase angle $3\pi/2$

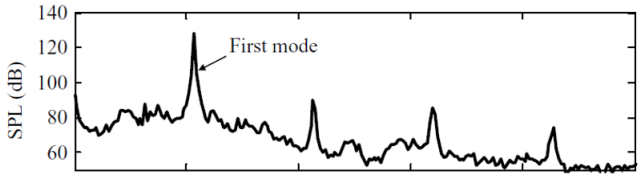

(a) SPL from Ma et al. experimental results

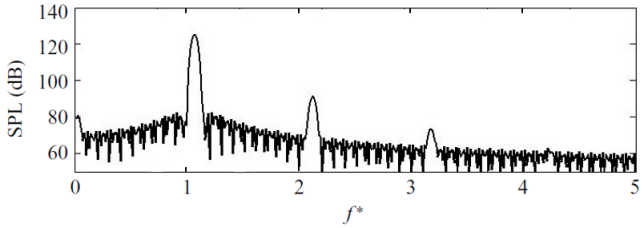

(b) SPL from computational results

Figure 3.7: Sound Pressure Level (SPL) results

each time step that contained the streamwise velocity and spanwise voricity of each point within the control volume. The resulting plot of the value for F^* as a function of time showed that while u and ω_z vary throughout the period of oscillation, the value of F^* stays nominally consistent.

To confirm accuracy of the frequencies seen in the computational model, the resulting sound pressure level (SPL) plot is compared to that of Ma et al.'s experimental study. Figure 3.7 displays SPL as a function of f^* at the free stream velocity of $U^* = 2.64$. General qualitative comparisons can be made between the experimental plot in Figure 3.7a from Ma et al.[9] and that from the computational model in Figure 3.7b. The peaks occur at nominally the same frequencies and there is good agreement between the maximum pressure levels of the first and second modes. Differences between the two plots can be attributed to the experimental data being continuous—recorded in real time using a microphone—whereas the computational model only records data at discrete time steps.

3.3 Grid Independence Study

A grid independence study was also performed to confirm the density of the grid was not impacting the results. This was achieved by increasing the density of the mesh until the computational solution converged with the known experimental value. Given the limitations in computational resource, the increase in density was focused on specific areas of the mesh. The main regions of interest, with respect to the flow regimes, are the wind tunnel floor and control volume around the orifice of the resonator. A coarser mesh was adequate in the remaining areas of the model, given the acoustic wavelength for the Helmholtz resonator is much larger than the dimensions of the resonator.

The layers of mesh in the wall normal direction from the wind tunnel floor are critical for accurate development of the boundary layer. The use of a RANS based turbulence model required a specific quantity of these mesh layers to operate correctly. Therefore, to alter the density in this region for the grid independence study, the mesh size was changed only in the streamwise and spanwise direction.

The second region of interest was surrounding the orifice, where the vortical structures roll up as they convect downstream, causing the oscillation of pressure within the resonator. It is these areas where the grid size becomes very small with respect to the other areas of the model. This is also where the primary mesh density changes were made during the grid independence study. Small changes were made to the remaining areas of the mesh to maintain appropriate growth ratios between the elements and to maintain adequate mesh quality levels, as discussed in the previous chapter.

To evaluate the results of each density change, the resulting P^* value was calculated and compared to the known experimental value. All of the simulations for the grid independence study were ran at

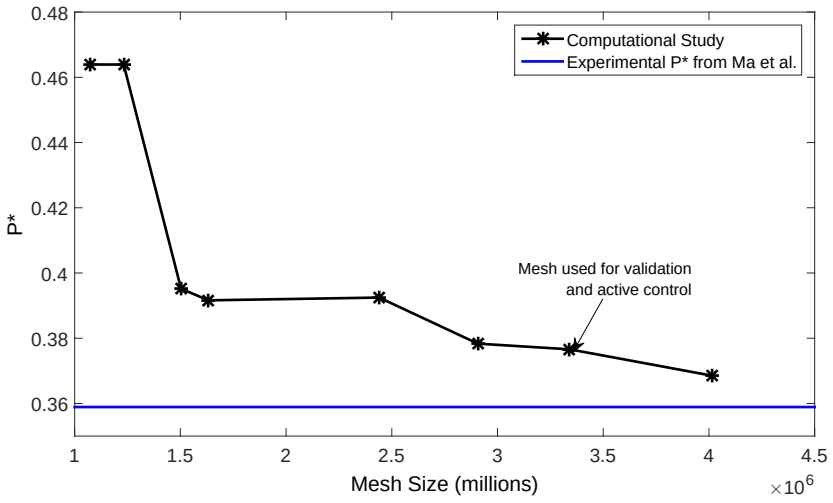

Figure 3.8: Grid independence study

the free stream veocity of $U^* = 2.64$. Figure 3.8 shows the results of the grid independence study, with the corresponding P^* value plotted as a function of the mesh density. The experimental value shown as a horizontal line is the P^* result obtained by Ma et al. using a microphone to record the pressure within the resonator.[9]

As the mesh density increases, the resulting P^* value approaches this experimental value. At the highest density (4,015,873 elements), the error between the computational and experimental results is 2.7%. Taking into account the need to manage computational resources, the mesh used for the validation study and active control research had 3,340,973 elements and an error of 4.1%. It is important to note however, that following the increase in mesh density to 1,503,285 elements the peak frequency of oscillations stayed constant at $f_{hr} = 47.8Hz$ throughout the remaining increase in density. For comparison, the experimental value obtained by Ma et al. is $f_{hr} = 46.0Hz$—a difference of 3.9%. This gave confidence in the accuracy of the mesh density chosen and its resulting solution.

4

Active Control

As the computational model and solver settings used in the CFD simulations were validated, the preliminary investigation into the use of active control followed with the desired results of reducing pressure oscillations within the resonator. In the practical application of an automobile, this would mean the elimination of the noise that can be produced when a side window or sunroof is opened. The peak pressure obtained in the validation study occurred at the non-dimensional free stream velocity

of $U^* = 2.64$. For the computational model this produces a specific free stream velocity of $15.2 m/s$, or $33.6 mph$. For a standard mid-size automobile the peak pressures would occur while traveling at $38.4 mph$. This is with an interior cabin volume of $3.25 m^3$ and sunroof opening measuring $2 ft$ in width and $1 ft$ in length. These results related well to the previously discussed study by Bai et al. who obtained peak pressures at a speed of $37 mph$.[5]

4.1 Addition of Mass Injection Jet

The active control method studied here—a single, constant speed air jet—is a simple, canonical flow that can provide a basic understanding of how the jet effects the shear layer and vorticity in the orifice region. The purpose of injecting air into the free stream flow is to mimic the effects of a physical ramp or step placed upstream of the orifice leading edge. With these passive control devices, the shear layer is effectively lifted above the opening of the resonator.[16] When the shear layer is further away from the orifice, it reduces the effects of the unsteady shear layer being coupled to the Helmholtz resonator acoustics.

Figure 4.1 depicts the location and geometry of the active control jet that was added to the model. In Figure 4.1a the jet is the white surface located on the wind tunnel floor. The center of the single rectangular slot jet was placed a distance of $x = 0.12L$ upstream of the resonator orifice leading edge. The jet has a spanwise dimension equal to that of the orifice and a streamwise length of $0.08L$.

Within the computational model the jet was simulated by defining its geometry on the wind tunnel floor and assigning an appropriate boundary condition for that geometry. This allowed the sim-

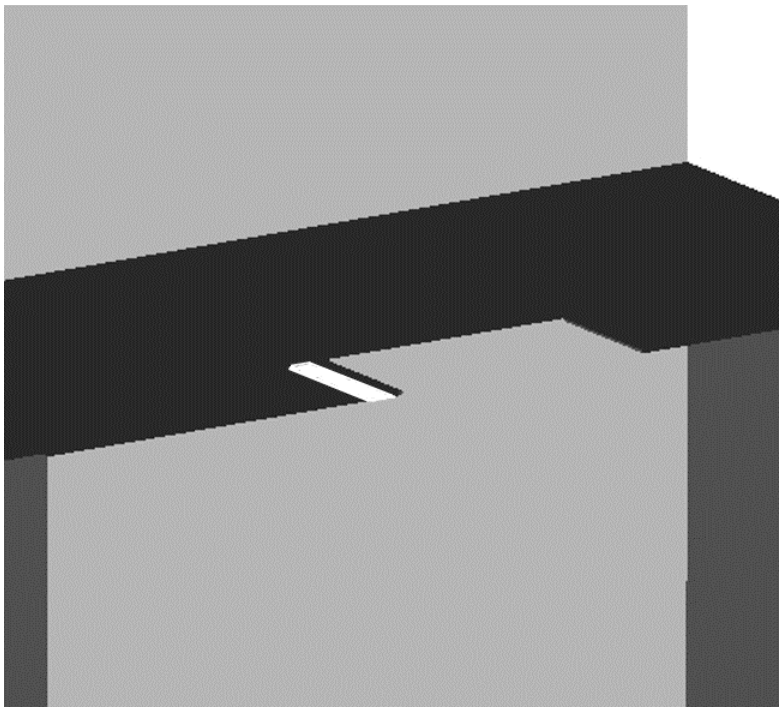

(a) Active flow control jet placed upstream of orifice

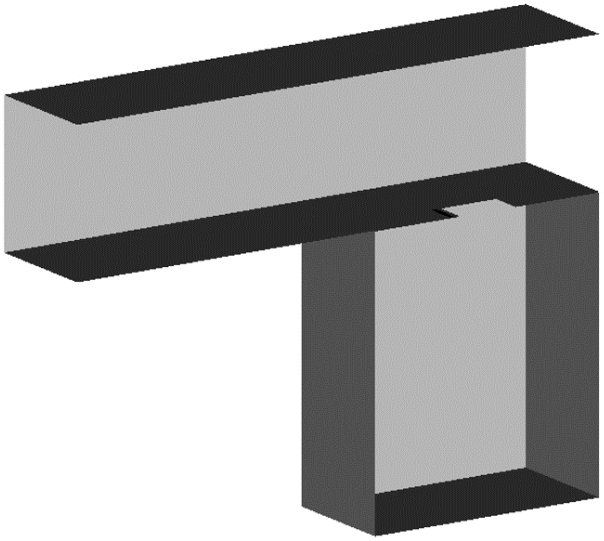

(b) Full 3d model with addition of jet

Figure 4.1: Updated computational model with active flow control jet

ulations to be run without active control by setting the jet boundary condition to a no-slip wall—matching that of the wind tunnel floor surrounding it. To enable the active control this boundary condition was changed to a velocity inlet. By defining the specific components of the velocity vector, both the magnitude and angle could be controlled. For this active control study the simulations were first run with the jet turned off, establishing the baseline pressure oscillations. Next, with all settings kept constant except for the jet's boundary condition, the simulation continued for an additional two seconds.

The computational study in the present work investigates multiple jet velocities but was limited to the single free stream velocity of $U^* = 2.64$. Peak resonator pressures are seen at this free stream velocity, allowing the active control to have the greatest effect. The angle of the jet was held constant at 45° from horizontal. This angle was chosen as a compromise between two desired effects of the jet with the first being to raise the shear layer above the resonator orifice. The second desired effect of imparting additional streamwise momentum to the flow, is an attempt to delay the onset of the vorticity rolling up into a discrete vortex.

It can be seen in Figure 4.2 how the velocity in the area of the orifice opening is effected when the jet is turned on. The shear layer that was previously at the same height as the orifice is lifted higher by the added mass air flow of the jet entering the boundary layer at a 45° angle. The vorticity is also being convected downstream across the orifice, delaying the point of rollup and reducing its corresponding impact on the pressure oscillations.

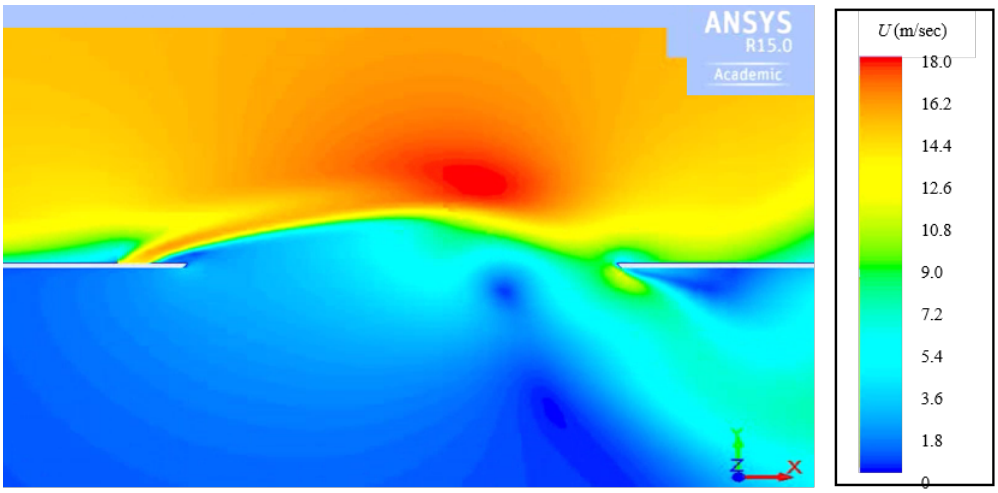

Figure 4.2: Streamwise velocity with active control jet

4.2 Results with Active Control

The results of the change in P^* using active control are shown in Figure 4.3, where U_{jet} is the jet velocity and a new term, the non-dimensional jet velocity, is defined as

$$U^*_{jet} = \frac{U_{jet}}{U}.$$

This term is kept in non-dimensional form to ease the ability of applying the results to any size or configuration of Helmholtz resonator. When $U^*_{jet} < 1.1$, the resulting reduction in resonator pressures are small (of the order of 5.0%). However, as the jet speed increases, the reduction in pressure levels increases as well. At the highest jet speed tested of $U^*_{jet} = 1.5$ there is a 72.2% reduction in P^*. This means for a free stream velocity of 15.2 m/s the jet velocity would be 22.8 m/s.

The contour plots in Figure 4.4 show both the spanwise vorticity in the area of the resonator orifice

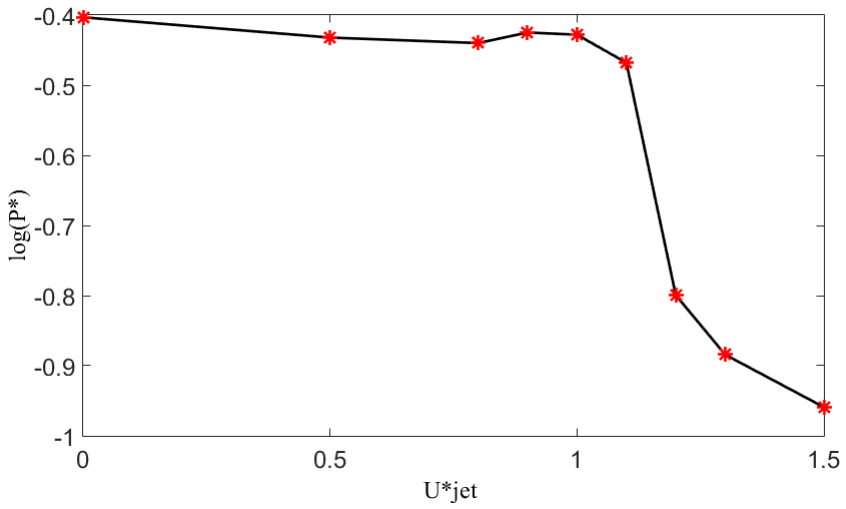

Figure 4.3: Active control P* Results

with the use of the active control jet. In Figure 4.4a it can be seen that despite the additional flow from the jet, the vorticity is still able to roll up into a discrete vortex prior to the downstream edge of the orifice. This is allowing the shear layer to remain coupled to the resonator. Figure 4.4b however shows a higher jet velocity of $U^*_{jet} = 1.5$ having a greater effect. The location where the the discrete vortex would form has moved further downstream, to the point where the orifice trailing edge is now preventing its full formation.

The actual resonator pressure for $U^*_{jet} = 1.5$ can be seen in Figure 4.5. Prior to activation of the jet, the magnitude of pressure fluctuations within the resonator reached a level of $160Pa$. Through the use of active control, those pressure fluctuations were reduced to less than $45Pa$. It can be observed that when running without active control the pressures oscillate around $0Pa$, whereas with active control the entire range of pressures remain negative.

With this specific size and location of jet, the active control is having two impacts on the shear

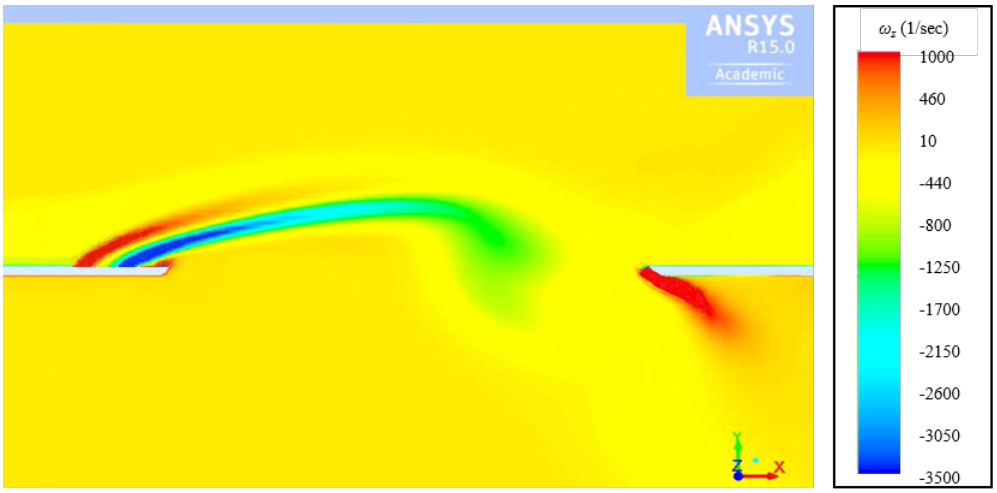

(a) $U^*_{jet} = 0.9$

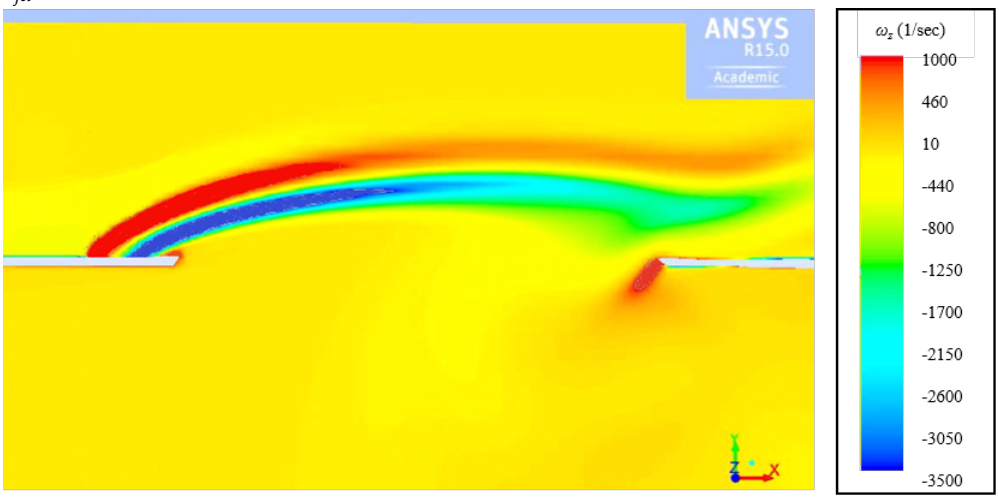

(b) $U^*_{jet} = 1.5$

Figure 4.4: Spanwise vorticity at phase angle $3\pi/2$ in orifice area with active control

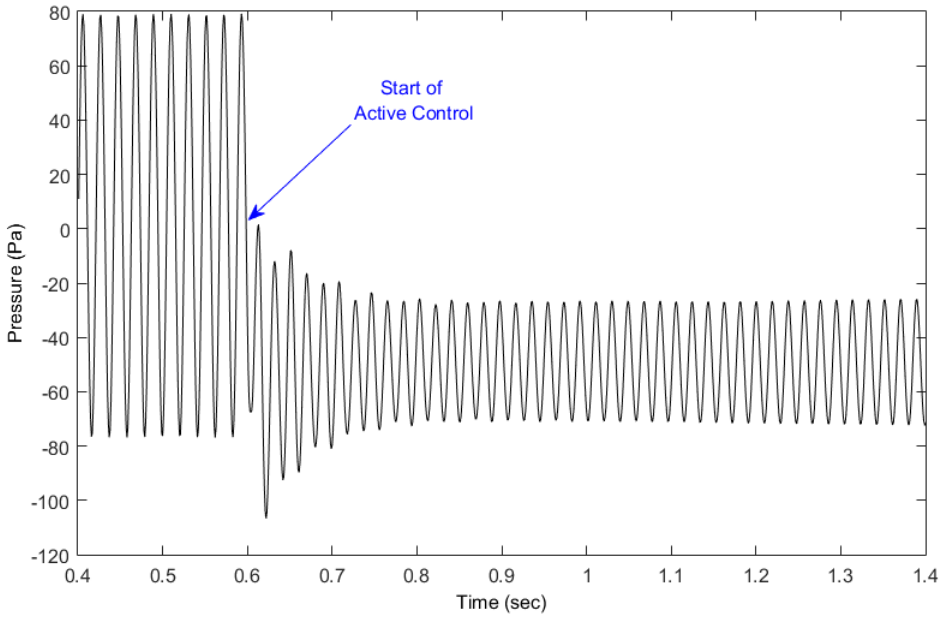

Figure 4.5: Resonator pressure at $U^* = 2.64$ and $U^*_{jet} = 1.5$

layer and vorticity. First, the addition of the air from the jet is having a similar effect as operating without active control but at a higher free stream velocity. In this situation the vorticity is not able to fully form a discrete vortex before reaching the orifice trailing edge. The second impact of the jet is in moving the shear layer higher up and away from the resonator orifice. This reduces the ability of the vorticity to force air into and out of the resonator as it convects downstream. It has the ultimate effect of decoupling the shear layer from the resonator acoustics, which eliminates the self-sustained oscillations.

5

Conclusion

5.1 Validation and Active Control

The results of the study that has been presented here provide a preliminary look into the use of air jets for the active control of a Helmholtz resonator. This was done by first validating both the computational model that was built and the applicable settings used by the CFD solver. The results from the validation study compared well to analytical and experimental results found in literature through

the use of three primary parameters—vorticity, P^*, and F^*. Additional qualitative comparisons were made by examining the vorticity contour plots of the computational study. The validation portion of this study has also shown the ability to use the RANS-based realizable $k - \varepsilon$ turbulence model, as opposed to an LES or hybrid-LES model, to reduce the computational resources needed for the simulations.

The active control study investigated multiple different jet velocities at a single angle of 45° and at the single free stream velocity of $U^* = 2.64$, where peak resonator pressures occur. With active control the resonator pressures were minimally reduced until the jet velocity reached a speed higher than $U^*_{jet} = 1.1$. Once above this level, the jet significantly reduced the peak pressures within the resonator. This success is attributed to the ability of the jet to raise the shear layer above the resonator orifice. It is also able to shift downstream the location where the vorticity rolls up into a discrete vortex. These effects are similar to the results when the simulations are run at higher free stream velocities without active control.

5.2 Applications to the Automobile and Future Work

While the purpose of the jets are to mimic the effects of a physical ramp, they are able to do so without the visual impact that would be had when applied to an automobile. Continued research will investigate changing additional characteristics of the jet and assessing possible negative impacts the jet may have when used in the automobile application. Further study using active control may also lead back to new ideas for passive control. Continuation of the current study will include optimizing the

computational model for off-peak U^* velocities and investigating why using active control produces negative resonator pressures.

The geometry used in the current study is a simple single slot jet. In relation to the automobile application—where placement of this jet would be on either an A-pillar, B-pillar, or on the roof just upstream of the sunroof—having a single slot jet the entire length of the opening would not be practical from a manufacturing or aesthetics perspective. A more practical design would be a series of smaller, individual jets placed along the leading edge of the window or sunroof opening. Another aspect that would need to be investigated is where the air for the jet would originate. The simplest approach could be to have a small intake duct located at the front of the vehicle that routes the incoming air to the jets. Given the jet velocities are similar to the free stream velocities, this could be a viable solution.

Other possible changes to the jet include its angle relative to the free stream flow and pulsing the jet(s) at specific frequencies relative to its corresponding Helmholtz frequency. Either of these changes would be in an attempt to lower the mass flow rate from the jet that is currently required to achieve the drop in sound pressure levels. Given the periodicity of the unsteady shear layer rolling up into discrete vortices, it is possible a jet pulsed at a specific frequency would reduce sound pressure levels further than what would be achieved with a jet at constant velocity. Addition of the jet may also cause unwanted effects that would need to be investigated. Specific to the automobile application, the flow from the jet could add unwanted drag and noise that could outweigh the benefit of reduced pressure levels within the cabin. However, the current study has shown with active flow control it is possible to lower the pressure oscillations of a Helmholtz resonator.

References

[1] (2013a). *Ansys Fluent Theory Guide*. Ansys Inc., Canonsburg, PA, release 15.0 edition.

[2] (2013b). *Ansys Fluent Tutorial Guide*. Ansys Inc., Canonsburg, PA, release 15.0 edition. pages 257-303.

[3] An, C. F., Puskarz, M., Singh, K., & Gleason, M. (2005). *Attempts for Reduction of Rear Window Buffeting Using CFD*. Technical Paper 2005-01-0603, SAE International, Warrendale, PA.

[4] Arunajatesan, S., Sinha, N., & Menon, S. (2000). Towards hybrid les-rans computations of cavityflowfields. In *AIAA 38th Aerospace Sciences Meeting and Exhibit*, AIAA-2000-0401 (pp. 1–10). Reston, VA: AIAA.

[5] Bai, I. H., Jo, Y. W., Lee, S. H., Moon, Y. J., Jeon, W. H., & Kim, J. I. (2013). Buffeting noise of automobile at running speeds. In *19th AIAA/CEAS Aeroacoustics Conference*, AIAA 2013-2181 Berlin, Germany: AIAA.

[6] Crouse, B., Senthooran, S., Balasubramanian, G., Freed, D., Swen, N., Mongeau, L., & Hong, J. (2005). *Sunroof Buffeting of a Simplified Car Model: Simulations of the Acoustic and Flow-induced Responses*. Technical Paper 2005-01-2498, SAE, Traverse City, MI.

[7] Davidson, P. A. (2004). *Turbulence: An Introduction for Scientists and Engineers*. New York, NY: Oxford University Press.

[8] Ghanadi, F., Arjomandi, M., Cassolato, B., & Zander, A. (2014). Understanding of the flow behavior on a helmholz resonator excited by grazing flow. *International Journal of Computational Fluid Dynamics*, 28(5), 219–231.

[9] Ma, R., Slaboch, P., & Morris, S. (2009). Fluid mechanics of the flow-excited helmholtz resonator. *Journal of Fluid Mechanics*, 623, 1–26.

[10] Mallick, S., Shock, R., & Yakhot, V. (2003). Numerical simulation of the excitation of a helmholtz resonator by a grazing flow. *The Journal of the Acoustical Society of America*, 114(4), 1833–1840.

[11] Mendoza, J. M. & Ahuja, K. K. (1996). Cavity noise control through upstream mass injction from a coanda surface. In *AIAA and CEAS Aeroacoustics Conference*, AIAA-96-1767 Washington, DC: AIAA.

[12] Mongeau, L., Franchek, M. K., & Kook, H. (1999). Control of interior pressure fluctuations due to flow over vehicle openings. In *Proceedings of the 1999 Noise and Vibration Conference*, 1999-01-1813 Warrendale, PA: SAE International.

[13] Pierce, A. (1989). *Acoustics: An Introduction to Its Physical Principles and Applications*. Melville, NY: Acoustical Society or America, third edition.

[14] Sarno, R. L. & Franke, M. E. (1994). Suppression of flow-induced pressure oscillations in cavities. *AIAA Journal of Aircraft*, 31(1), 90–96.

[15] Shih, T., Liou, W., Shabbir, A., Yang, Z., & Zhu, J. (1995). *A New k-epsilon Eddy Viscosity Model for High Reynolds Number Turbulent Flows: Model Development and Validation*. Technical Memorandum NASA-TM-106721, NASA, Cleveland, OH.

[16] Slaboch, P. E. (2009). *Fluid Mechanics and Passive Control of the Flow-Excited Helmholtz Resonator*. PhD thesis, University of Notre Dame, Notre Dame, IN.

[17] Vakili, A. D., Wolfe, R., Nagle, T., & Lambert, E. (1995). Active control of cavity aeroacoustics in high speed flows. In *AIAA 33rd Aerospace Sciences Meeting and Exhibit*, AIAA-95-0678 Washington, DC: AIAA.

[18] Voorhees, C. G. & J., B. J. (1969). Effect of upstream mass injection on the pressure field in a cavity. *AIAA Journal*, 7(4), 747–749.

[19] Zhendong, Y., Zhengqi, G., Jiyuan, T., Guangping, D., & Yiping, W. (2014). Numerical analysis and passive control of a car side window buffeting noise based on scale-adaptive simulation. *Applied Acoustics*, 79, 23–34.